Phosphorous incorporation in Pd_2Sn alloys for electrocatalytic ethanol oxidation

Xiaoting Yu[a,b], Junfeng Liu[c,*], Junshan Li[d], Zhishan Luo[e,f], Yong Zuo[a,b], Congcong Xing[a,g], Jordi Llorca[f], Jordi Arbiol[h,i], Kai Pan[j], Ying Xie[j,*], Andreu Cabot[a,i,*]

a Catalonia Institute for Energy Research - IREC, Sant Adrià de Besòs, 08930 Barcelona, Spain

b Department of Electronic and Biomedical Engineering, Universitat de Barcelona, 08028 Barcelona, Spain

c Institute for Energy Research, School of Chemistry and Chemical Engineering, Jiangsu University, 212013 Zhenjiang, P.R. China

d Institute of Fundamental and Frontier Sciences, University of Electronic Science and Technology of China, 610054 Chengdu, P. R. China

e Department of Chemistry, Southern University of Science and Technology (SUSTech),518055 Shenzhen, Guangdong, P. R. China

f SUSTech Academy for Advanced Interdisciplinary Studies, Southern University of Science and Technology (SUSTech), 518055 Shenzhen, Guangdong, P. R. China

g Institute of Energy Technologies, Department of Chemical Engineering and Barcelona Research Center in Multiscale Science and Engineering, Universitat Politècnica de Catalunya, EEBE, 08019 Barcelona, Spain

h Catalan Institute of Nanoscience and Nanotechnology (ICN2), CSIC and BIST, Campus UAB, Bellaterra, 08193 Barcelona, Spain

i ICREA, Pg. Lluís Companys 23, 08010 Barcelona, Spain

j Key Laboratory of Functional Inorganic Material Chemistry, Ministry of Education, Heilongjiang University, 150080 Harbin, P.R. China

ABSTRACT

Direct ethanol fuel cells (DEFCs) show a huge potential to power future electric vehicles and portable electronics, but their deployment is currently limited by the unavailability of proper electrocatalysis for the ethanol oxidation reaction (EOR). In this work, we engineer a new electrocatalyst by incorporating phosphorous into a palladium-tin alloy and demonstrate a significant performance improvement toward EOR. We first detail a synthetic method to produce Pd_2Sn:P nanocrystals that incorporate 35 % of phosphorus. These nanoparticles are supported on carbon black and tested for EOR. Pd_2Sn:P/C catalysts exhibit mass current densities up to 4.89 A mg_{Pd}^{-1}, well above those of Pd_2Sn/C, PdP_2/C and Pd/C reference catalysts. Furthermore, a twofold lower Tafel slope and a much longer durability are revealed for the Pd_2Sn:P/C catalyst compared with Pd/C. The performance improvement is rationalized with the aid of DFT calculations considering different phosphorous chemical environments. Depending on its oxidation state, surface phosphorus introduces sites with low energy OH^- adsorption and/or strongly influences the electronic structure of palladium and tin to facilitate the oxidation of the acetyl to acetic acid, which is considered the EOR rate limiting step.

Keywords: Palladium; Electrocatalysis; Phosphide; Nanoparticle; Ethanol oxidation reaction

1. Introduction

Direct liquid fuel cells provide a means for the straight conversion of chemical energy within a liquid fuel into electricity. Among possible liquid fuels, ethanol offers a large energy density (8.01 KWh kg^{-1}), low toxicity, relatively high boiling point for safe storage, transportation and operation, and potential for bio-sourcing [1,2]. These advantages make direct ethanol fuel cells (DEFCs) extremely appealing to power electric vehicles and portable electronics, among other applications. However, the deployment of DEFCs is being hampered by the high cost and moderate performances of current electrocatalysts for the ethanol oxidation reaction (EOR) [3].

Pt and Pt-based alloys have been the most studied and optimized EOR catalysts to date, particularly in acidic conditions, but their high cost limits their application [4]. Compared with acid electrolytes, alkaline solutions are less corrosive and provide faster reaction kinetics for both alcohol oxidation and oxygen reduction, which enable the use of a larger variety of catalysts [5]. These advantages together with the development of high-performance anion exchange membranes, have moved interest from acid- to basic-type DEFCs and from Pt to less costly catalysts. Moving away from Pt-based catalysts, increasing attention is being paid to Pd alloys, which offer lower cost, better resistance to poisoning and similar or even better catalytic activities [6-8]. We and others have recently demonstrated that alloying Pd with Sn and optimizing the catalyst crystallographic facets significantly improve EOR performances through a combination of electronic and bifunctional effects [9-12]. We have also recently reported that the incorporation of phosphorous into Pd catalysts affords several advantages toward EOR activity [13]. Phosphorous inclusion provides additional adsorption sites [14,15], slightly modifies the electronic structure of Pd [16], shifts the Pd oxide formation to higher potentials that in turn results in a better stability [17], and reduces the amount of Pd required to reach a certain operation current, thus further reducing the overall catalyst cost [15,18-24].

Herein we report an approach to prepare the first Pd-based catalyst that incorporate both elements, Sn and P. We produced Pd_2Sn:P by reacting intermetallic Pd_2Sn with a phosphorous precursor during the nanoparticle growth stage. These particles were supported on carbon black and tested toward ethanol oxidation in alkaline media. DFT calculations were used to identify the relationship between the measured performances and the catalyst composition.

2. Material and methods

2.1. Chemicals

Oleylamine (OAm, 80–90%) was purchased from ACROS Organics. 1-Octadecene (ODE, 90%), palladium(II) acetylacetonate ($Pd(acac)_2$, Pd 34.7wt%), tin(II) acetate ($Sn(OAc)_2$, 99%), hexamethylphosphorous triamide (HMPT, 97%), trioctylphosphine (TOP, 97%), methylamine hydrochloride (MAC, 98%), potassium hydroxide (KOH, 85%), and Nafion (5 wt% in a mixture of low aliphatic alcohols and water) were obtained from Sigma-Aldrich. A reference Pd catalyst, 20% Pd on activated carbon powder, was purchased from Alfa Aesar. Carbon black Vulcan XC-72 was obtained from Fuel Cell Earth. Hexane, ethanol and acetone were of analytical grade and obtained from various sources. MilliQ water was obtained from a PURELAB flex from ELGA. All chemicals were used as received, without further purification.

2.2. Synthesis of Pd_2Sn:P

91.4 mg (0.3 mmol) of $Pd(acac)_2$, 35.5 mg (0.3 mmol) of $Sn(OAc)_2$ and 68.0 mg (1 mmol) of MAC were mixed with 20 mL of OAm in a 50 mL three-neck flask connected to the Schlenk line coupled to an exhaust gas absorption solution (1 M $CuSO_4$). After keeping the precursor mixture under argon flow for 15 min, 1 mL of TOP was introduced. Subsequently, the solution was heated to 100 °C and maintained at this temperature for 1 h. Then temperature was slowly increased to 200 °C at a rate of 5 °C/min and maintained for 30 min. Next, temperature was increased to 300 °C in 40 min. During this temperature increase, the solution turned black indicating the nucleation of Pd-Sn nanocrystals [25]. When the solution reached 300 °C, 0.2 mL (1.1 mmol) of HMPT dissolved in 0.5 mL of ODE was injected and the mixture was allowed to react for 1 h before cooling down to ambient temperature. The reaction product was precipitated by adding excess amount of acetone and centrifugation at 5000 rpm for 5 min. Then, it was re-dispersed and re-precipitated 3 times with chloroform and acetone. The final black product was dispersed in hexane.

2.3. Synthesis of reference nanocrystals: Pd_2Sn and PdP_2

Pd_2Sn nanorods were produced following the exact same protocol described above but without adding HMPT at 300 °C [25]. PdP_2 nanocrystals were obtained through the same procedure but without adding $Sn(OAc)_2$ to the initial precursor solution [13]. Nanoparticles were purified as detailed above and the final black precipitates were dispersed in hexane.

2.4 Catalysts preparation

Pd_2Sn:P/C, Pd_2Sn/C and Pd_2P/C electrocatalysts were prepared by supporting the corresponding nanocrystals on carbon black [26]. Briefly, 5 mg of Pd_2Sn:P (or Pd_2Sn/Pd_2P) dispersed in 5 mL of hexane were mixed with 5 mg of Vulcan XC-72 carbon dispersed in ethanol. The mixture was sonicated for 1 h to homogeneous distribute the nanocrystals over the carbon surface. The product was collected by centrifugation and then dispersed in a mixture of 10 mL ethanol and 1 mL acetic acid to remove surface

organic ligands through sonication. After washing with ethanol, the catalyst was dried naturally under ambient condition and then it was annealed at 250 °C in Ar atmosphere for 1h. The final product was dispersed in isopropanol containing 5% Nafion to obtain an ink containing a nanocrystal concentration of 1 mg/mL.

2.5 Electrochemical measurements.

Electrochemical measurements were conducted at room temperature with a BioLogic electrochemical workstation using a three-neck-type cell including a Pt gauze as counter electrode and a Hg/HgO (1 M KOH) electrode as reference. The working electrode was prepared by drop-casting 3 μL of the catalyst ink on a 5 mm diameter glassy carbon (GC) electrode and letting it dry naturally. The same mass of particles (or Pd for the commercial sample) was used to prepare each electrode, which translated into lower amounts of Pd on the Pd_2Sn:P/C catalyst when compared with the 3 reference catalysts tested. Cyclic voltammetry (CV) curves were recorded at a scan rate of 50 mV s^{-1} in Ar-saturated aqueous solutions that contained 0.5 M KOH or 0.5 M KOH + 0.5 M ethanol. Chronoameperometry (CA) measurements were conducted at -0.1 V vs. Hg/HgO for 7000 s in a 0.5 M KOH + 0.5 M ethanol electrolyte.

2.6 Structural and chemical characterization

Powder X-ray diffraction (XRD) patterns were collected from the samples supported on a Si substrate on a Bruker-AXS D8 Advanced X-ray diffractometer with Ni-filtered (2 μm thickness) Cu K radiation (λ=1.5406 Å) operating at 40 kV and 40 mA. Scanning electron microscopy (SEM) analysis was conducted with a ZEISS Auriga microscope equipped with an energy dispersive X-ray spectroscopy (EDS) detector operating at 20 kV. Transmission electron microscopy (TEM) images were carried out with a ZEISS LIBRA 120 operating at 120 kV and a JEOL 1011 at 100 kV. High-resolution TEM (HRTEM) analysis was carried out using a field emission gun FEI™ Tecnai F20 microscope at 200 kV with a point-to-point resolution of 0.19 nm. Annular dark-field scanning transmission electron microscope (HAADF-STEM) was combined with electron energy loss spectroscopy (EELS) in the Tecnai F20 with a GATAN QUANTUM filter. X-ray photoelectron spectroscopy (XPS) was analyzed on a SPECS system equipped with an Al anode XR50 source operating at 150 W and a Phoibos 150 MCD-9 detector. The pressure of the analysis chamber was below 10^{-7} Pa. The CasaXPS program (Casa Software Ltd., UK) was employed for the data process.

2.7 Computational details

All calculations were performed using the Vienna Ab initio Simulation Package (VASP) [27-30] within the density functional theory (DFT) framework. Perdew-Burke-Ernzerhof (PBE) functional [31] was used to treat the exchange-correlation energy. The projector augmented-wave (PAW) [32] was applied and the energy cutoff was 400 eV. The sampling over Brillouin zone was treated by the Monkhorst-Pack technique

[33], and a (2×2×1) grid was introduced. Geometry optimization process was repeated until the energy change of two adjacent ionic steps is less than 10^{-5} eV and the force on the atoms less than -0.03 eV/Å. Furthermore, dispersion interactions were treated on the DFT-D3 level [34,35]. During the calculation, the (2×2×1) supercells for Pd_2Sn (001) and P-modified surfaces were used and displayed in Fig. S1. A vacuum slab of 15 Å was applied to avoid the pseudo interactions between the periodic images along z axis. The adsorption energies for OH^- on different sites of the surfaces were calculated based on the following equation

$$E_{ad.} = E_{OH/slab} - E_{OH^-} - E_{slab} \qquad (1)$$

where $E_{OH/slab}$, E_{OH^-}, and E_{slab} are the total energies for OH/slab, OH^-, and the pure surface, respectively. Furthermore, the energy of OH^- was calculated by equation [36]

$$E(\mathrm{OH^-}) = E(\mathrm{H_2O}) - [\frac{1}{2}E(\mathrm{H_2}) - PH \times k_B T ln10] \qquad (2)$$

3. Results and discussion

3.1 Pd_2Sn:P nanorods

Fig. 1a displays a representative TEM micrograph of the particles obtained from the reaction of $Pd(acac)_2$ and $Sn(OAc)_2$ within OAm, MAC and TOP and the posterior phosphorization step at 300 °C using HMPT (see details in the experimental section). The produced nanoparticles displayed elongated morphologies with an average length and width of (24 ± 3) × (9 ± 1) nm (Fig. 1a inset). This morphology resembled that of Pd_2Sn nanorods produced following the same strategy but without the addition of HMPT [25]. The XRD pattern of the particles displayed an orthorhombic phase with space group Pnma, matching the reference pattern from Pd_2Sn (JCPDS 01-089-2057). No evidence of additional diffraction peaks corresponding to secondary phases such as Pd_5PSn, PdP_2 or SnP, was observed. HRTEM analysis confirmed the orthorhombic (S.G.: Pnma) Pd_2Sn phase with lattice parameters: a = 5.6500 Å, b = 4.3100 Å, c = 8.1200 Å (Fig. 1c). STEM-EELS elemental compositional maps unequivocally displayed the presence of Pd, Sn and P evenly distributed throughout the purified nanorods (Fig. 1d). EDS analysis confirmed the presence of P and allowed to quantify the overall elemental ratios as Pd/Sn/P = 2.1/1.0/2.2. To determine the amount of P present as a ligand at the surface of Pd_2Sn nanocrystals, samples were annealed under argon at 400 °C for 1 h. After this process, EDS analysis showed a 23% decrease of the phosphorus concentration: Pd/Sn/P = 2.1/1.0/1.7. We thus assume that the final Pd_2Sn:P crystals incorporate ca. 35 % of strongly bond phosphorous. This phosphorus is incorporated upon the reaction of the Pd_2Sn nuclei with HMPT and is accommodated within the Pd_2Sn lattice either at interstitials, partially replacing Pd and or Sn or in part preferentially bond at surface sites.

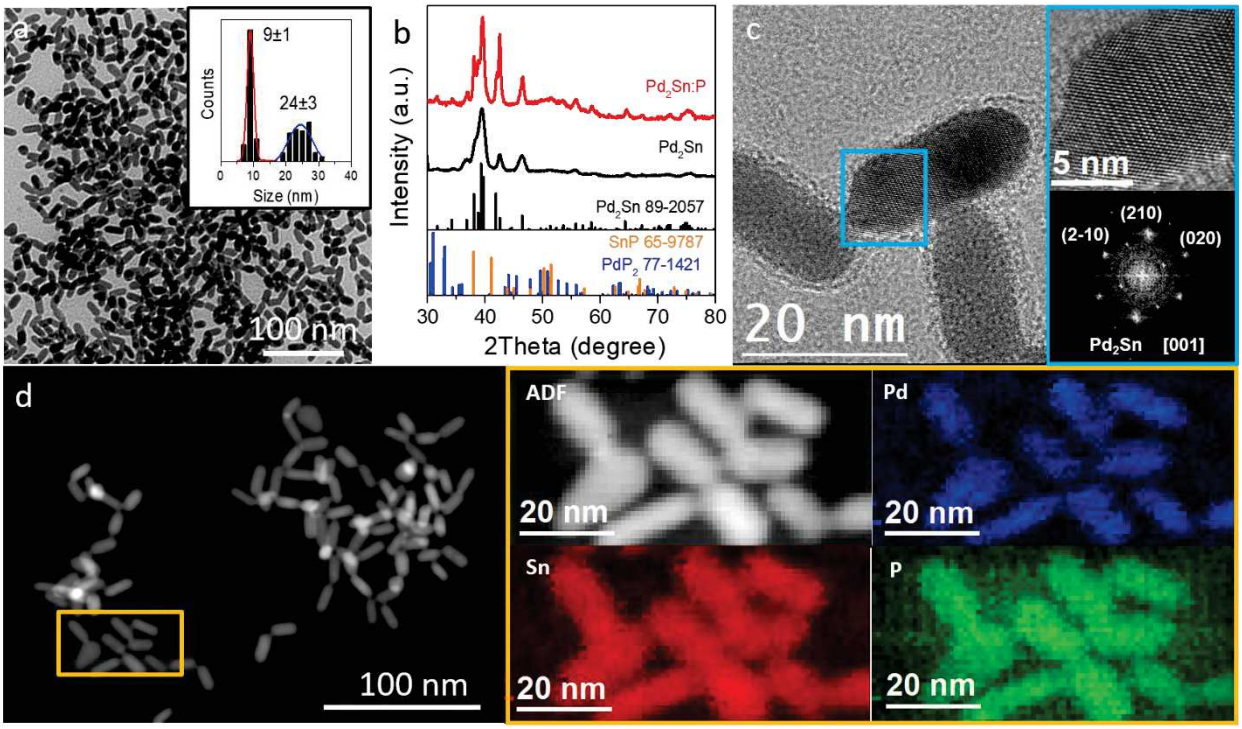

Fig. 1. (a) TEM micrograph and histograms of the length (blue) and width (red) distribution of Pd_2Sn:P nanorods. (b) XRD patterns of Pd_2Sn:P and Pd_2Sn nanorods. (c) HRTEM micrograph of Pd_2Sn:P nanorods and power spectrum (FFT) of a particle visualized along its [001] zone axis. (d) HAADF-STEM micrograph of Pd_2Sn:P nanorods and STEM – EELS elemental composition maps from the orange square area: Pd (blue), Sn (red) and P (green).

Fig. 2 displays the XPS spectra of purified Pd_2Sn:P nanocrystals and a Pd_2Sn:P/C catalyst. To prepare the catalysts, Pd_2Sn:P particles were supported on carbon black and treated with acetic acid to displace organic ligands (see material and methods section for details). The Pd 3d spectrum of the purified Pd_2Sn:P nanorods exhibited one doublet at 335.4 ($3d_{5/2}$) and 340.6 eV ($3d_{3/2}$) that was assigned to a Pd^0 chemical environment (Fig. 2a) [37,38]. After preparing the catalyst, a second doublet appeared at 337.4 eV ($3d_{5/2}$) and 342.6 eV ($3d_{3/2}$) as shown in Fig. 2b. This doublet was ascribed to a Pd^{2+} chemical state and accounted for ca. 14 % of the probed surface Pd [37]. The appearance of this oxidized component was associated with the exposure of the unprotected nanoparticles surface to ambient atmosphere during manipulation and transportation.

The Sn 3d spectra indicated the presence of two chemical states already in the purified Pd_2Sn:P nanoparticles, before ligand displacement (Fig. 2a). A first doublet at 484.6 eV (Sn $3d_{5/2}$) and 493.0 eV (Sn $3d_{3/2}$) was assigned to Sn^0 and accounted for 32 % of the probed Sn [37,38]. The second doublet, located at 486.6 eV (Sn $3d_{5/2}$) and 495.0 eV (Sn $3d_{3/2}$), was assigned to an oxidized Sn component, Sn^{x+} [37]. After

supporting the nanoparticles on carbon black and displacing the ligands, the oxidized Sn component increased up to the 77 % of the total Sn probed (Fig. 2b).

Two phosphorous chemical states were also identified from the XPS analysis of the purified Pd_2Sn:P nanoparticles, before ligand displacement (Fig. 2a). The XPS peaks at lower binding energy, at 130.0 eV (P $2p_{3/2}$) and 130.9 (P $2p_{1/2}$), were assigned to P within a metal phosphide lattice [16,37]. It was not possible to further distinguish the exact metal phosphide environment. The second phosphorous chemical state, at 133.1 eV (P $2p_{3/2}$) and 134.0 (P $2p_{1/2}$), was assigned to an oxidized phosphorous environment that we tentatively identified as a phosphate $(PO_4)^{3-}$ [16,37,39]. The oxidized component accounted for ca. 65 % of the total P observed. When supported on carbon black and after ligand displacement, only the oxidized component was observed (Fig. 2b).

The Pd_2Sn:P surface atomic ratio, as determined by XPS, was Pd/Sn/P = 1/0.97/1.37. Therefore, taking into account EDS data, the surface of Pd_2Sn:P nanorods was Sn- and P-rich. This result correlated well with the higher percentages of oxidized tin and phosphorous obtained. The Sn-rich surface might be related to the higher tendency of this element to oxidize under ambient atmosphere compared with Pd and it is consistent with results obtained for Pd_2Sn, with an XPS elemental ratio of Pd/Sn = 1.2 [25]. On the other hand, the surface of PdP_2 particles was reported to be Pd-rich [16], thus the higher percentage of P obtained on the surface of Pd_2Sn:P, with respect to Pd but not to Sn, may be related either to a preferential accommodation of P in the crystal surface or a differential diffusion/redistribution of phosphorous and palladium upon surface oxidation within a Pd_2Sn lattice when compared with the PdP_2 lattice.

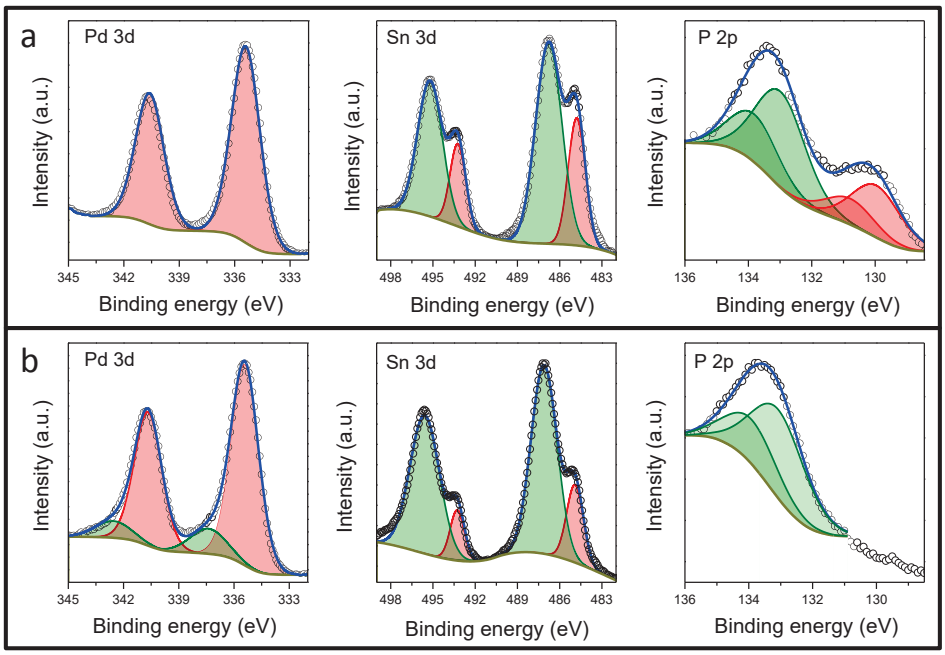

Fig. 2. XPS spectra of Pd, Sn and P from Pd_2Sn:P nanorods (a) and the Pd_2Sn:P/C catalyst (b).

3.2 Electrocatalytic ethanol oxidation

Fig. 3a displays CV curves recorded after 30 activation cycles. The current density peaks in the region between -0.5 V and -0.9 V vs. Hg/HgO were attributed to hydrogen adsorption in the cathodic scan and desorption in the anodic scan.[40],[41] The current density peaks at ca. -0.2 V vs. Hg/HgO in the forward scan were associated with the oxidation of surface Pd. During the reverse scan, clear PdO reduction peaks were identified at around -0.2 V vs. Hg/HgO.

The electrochemical active surface area (ECSA) of the catalysts was estimated from the coulombic charge associated with the PdO reduction peak:

$$\mathrm{ECSA} = \frac{\mathrm{Q}\ (\mu C \cdot cm^{-2})}{Q_{PdO}(\mu C \cdot cm_{Pd}^{-2}) \times Pd_{loading}(mg \cdot cm^{-2}) \times 10}$$

where Q_{PdO} = 405 μC cm^{-2} was the charge associated to the reduction of a PdO monolayer, the coulombic charge Q was calculated by integrating the area of the PdO reduction peak, and the Pd loading was the amount of Pd on the working electrode [12]. Using this equation, ECSA values for Pd/C, PdP_2/C, Pd_2Sn/C and Pd_2Sn:P/C catalysts were 50.7 m^2g^{-1}, 61.1 m^2g^{-1}, 76.8 m^2g^{-1}, and 116.8 m^2g^{-1}, respectively. Notice that significantly larger ECSAs were obtained with the addition of Sn and P to Pd, and the highest ECSA was obtained when simultaneously incorporating both elements to obtain the Pd_2Sn:P/C catalyst.

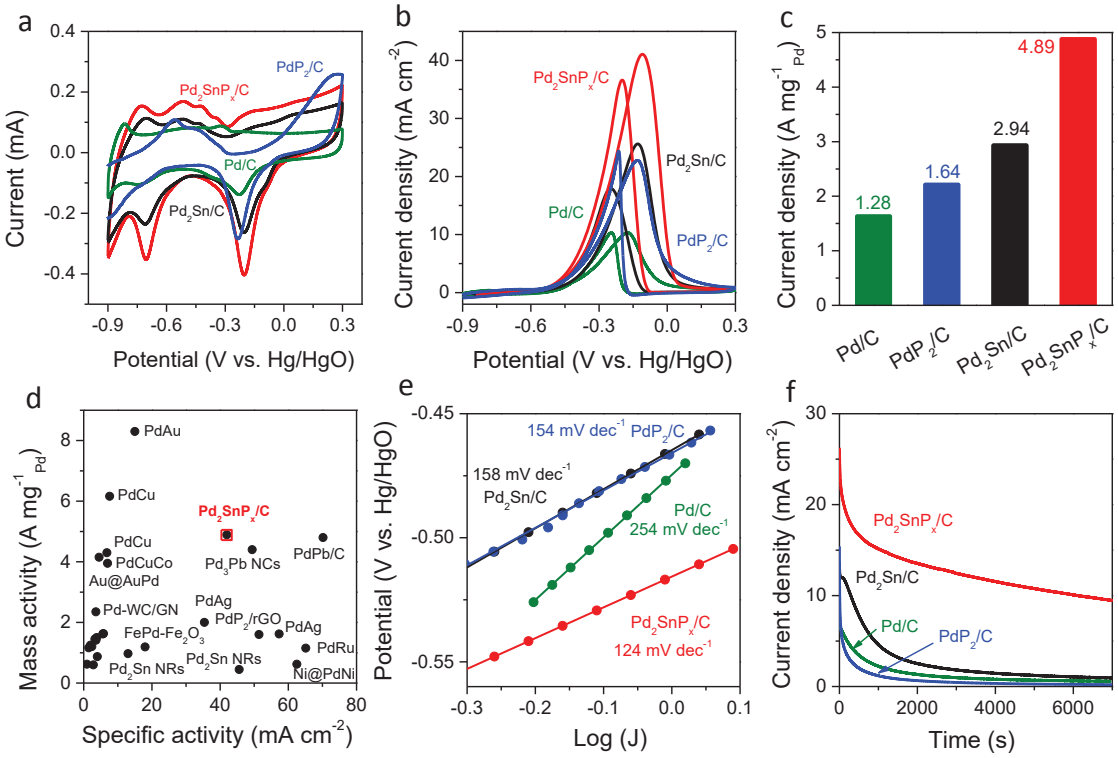

Fig. 3. (a) CV curves (after 30 stabilization cycles) of Pd_2Sn:P/C, Pd_2Sn/C, PdP_2/C and commercial Pd/C catalysts in 0.5 M KOH aqueous solution. (b) CV curves and (c) mass peak current density of Pd_2Sn:P/C,

Pd_2Sn/C, PdP_2/C and commercial Pd/C catalysts in 0.5 M KOH + 0.5 M EtOH aqueous solution. (d) Mass current density and specific current density of Pd_2Sn:P/C compared with Pd-based catalysts reported in the literature. (e) Tafel plots and (f) CA data of Pd_2Sn:P/C, Pd_2Sn/C, PdP_2/C and commercial Pd/C catalysts at −0.1 V vs. Hg/HgO in 0.5 M KOH + 0.5 M EtOH aqueous solution.

Fig. 3b displays the CV curves of the electrocatalysts in 0.5 M KOH + 0.5 M EtOH solution. The characteristic ethanol oxidation peaks were identified in the anodic and reverse scans for all the electrocatalysts tested. In the forward scan, the current density associated with the EOR started rising at ca. -0.55 V vs. Hg/HgO for all samples, and reached a maximum at a potential in the range from -0.10 V to -0.17 V vs. Hg/HgO, depending on the catalyst composition. Above these potentials, the current density decreased due to the surface oxidation of palladium. The catalyst containing phosphorous and/or tin displayed peaks at slightly higher potentials than the Pd/C catalyst. In the reverse scan, a sharp rise in the current density was triggered by the reduction of PdO at a voltage range between -0.08 V vs. Hg/HgO for Pd_2Sn:P/C and -0.18 V for Pd/C. The presence of Sn and P promoted the EOR activity and best performance was obtained when both elements were alloyed together with Pd. Pd_2Sn:P/C catalyst was characterized by the highest peak current density up to 41.2 mA cm^{-2}, compared with the 25.5 mA cm^{-2} for Pd_2Sn/C, 22.5 mA cm^{-2} for PdP_2/C and 10.3 mA cm^{-2} for Pd/C. These values resulted in dramatically high mass current densities for Pd_2Sn:P/C, up to 4.89 A mg_{Pd}^{-1} (Fig. 3c). Fig. 3d compares the specific and mass activities of Pd_2Sn:P/C with reported Pd-based catalysts showing that the simultaneous incorporation of Sn and P effectively improved the Pd activity toward EOR [9,12,16,42-58]. Additionally, the potential increase required to rise the current density was also significantly low for Pd_2Sn:P/C, especially when compared with commercial Pd/C, as noted in the Tafel plots displayed in Fig. 3e.

The electrocatalyst long-term stability was evaluated by chronoamperometry measurements (Fig. 3f). All the catalysts showed a sharp current density decay during the first 1000 s, which was ascribed to the surface accumulation of strongly adsorbed intermediates that partially blocked the active sites. The Pd_2Sn:P/C catalyst showed a lower decay and was able to maintain much higher current densities during the whole chronoamperometric test, displaying very high current densities of 9.52 mA cm^{-2} even after 7000 s operation.

3.3 DFT Calculations

To evaluate the effect of phosphorus, DFT calculations were carried out (computational details and models can be found on the material and methods section and the supporting information). According to previous literature, in alkaline media, EtOH is dehydrogenated into adsorbed acetyl, which is further oxidized to acetate by hydroxide species. The oxidation of the acetyl to acetic acid by adsorbed hydroxyl

is regarded as the rate-limiting step, while the stripping of the acetic acid in the form of acetate ions in alkaline solution is very rapid [59,60]. We calculated the OH^- adsorption energies at different sites of the catalysts surface (Table 1) and related these values to the catalyst activity considering that a higher chemical adsorption of OH^- allows increases activity by facilitating the formation of CH_3COOH [61]. For a pure Pd_2Sn surface used as a reference, the average Bader charges for Pd and Sn species at the topmost layer were -0.282 and +0.596, respectively. As a result, the adsorption of OH^- at Sn sites should be more energetically favorable than at Pd sites. Additionally, according to the optimized geometries, OH^- tends to be located at the bridge or center but not at the top sites, i.e. Sn-Pd bridge, Pd-Pd bridge, and Pd_3 center. Due to the slightly different Bader charges, the adsorption energies for the bridge site of Sn-Pd dimers varies slightly with an average value of -0.821 eV. Furthermore, in consideration of the large difference in adsorption energies between Pd- and Sn-relevant sites and the opposite charges, the selective adsorption of CH_3CO radicals near Pd site and that of OH^- near Sn ones is to be expected, which also benefits the catalytic reaction. These results are consistent with improved EOR catalytic performances obtained for Pd_2Sn with respect to Pd [38].

When introducing phosphorus into the system, two representative models were considered (Fig. S1b and 1c). A first model assumed the incorporation of P within the Pd_2Sn lattice with a phosphide environment. A second model considered the presence of oxidized P on the catalyst surface, in accordance with XPS results. In the first model, the Bader charges of Pd near P increased slightly, while those of Sn remained nearly unchanged, as observed in the EDD diagram (Fig. S2). In this model, the adsorption energies of OH^- at different sites decreased to a certain extent, which facilitated overcoming the EOR rate-limiting step. However, the lowest adsorption energies corresponded to the adsorption of OH^- on top of the surface P. In a second model, we considered the presence of P oxidized species, PO_x, on the catalyst surface (Fig. S1c). In this configuration Sn ions close to P are oxidized to a much higher valence state, and an electron transfer is clearly observed (Fig. S3c). These significant changes in electronic structures lead to a major decrease of the adsorption energies for OH^- (Table 1), which we believe favored boosting the catalytic activity of the material. Additionally, the promotion of the OH^- adsorption also favored the oxidation of poisoning species, thus increasing the catalyst stability.

Table 1. Adsorption energies for OH^- on different sites of Pd_2Sn and Pd_2Sn:P surfaces, considering two sites and chemical states of P.

	Sn-Pd bridge	Pd-Pd bridge	Pd_3 center	P top
Pd_2Sn	-0.821	-0.501	-0.499	–
Pd_2Sn incorporating P	-0.851	-0.552	-0.580	-0.925
Pd_2Sn incorporating surface PO_x	-1.041	-0.560	-0.658	–

4. Conclusions

We demonstrated the synthesis of colloidal Pd_2Sn:P nanorods through phosphorization of Pd_2Sn nanocrystals with a highly active reagent-HMPT in a one-pot two-steps reaction. Pd_2Sn:P/C catalyst exhibited significantly enhanced activity toward EOR in alkaline media compared with Pd_2Sn/C, PdP_2/C and commercial Pd/C catalysts. The introduction of P additionally improved the durability of Pd_2Sn:P/C catalyst and resulted in lower Tafel slopes that denoted a larger density of active sites. DFT calculations showed that the incorporation of phosphorous either as lattice P or as a surface phosphate, allowed reducing the OH^- adsorption energy both through an electronic effect and a direct bifunctional role, thus contributing to overcome the rate limiting step in EOR and increasing the rate of oxidation of poisoning species.

Author information

Corresponding authors

*E-mail: jliu@ujs.edu.cn (J.L.).

*E-mail: xieying@hlju.edu.cn (Y.X.).

*E-mail: acabot@irec.cat (A.C.).

Author contributions

This manuscript was prepared with the contribution of all the authors. A. Cabot and J. Liu conceived the project, guided and supervised the work. X. Yu designed the experiments, produced all the materials, conducted most of the characterization and the electrochemical measurements. J. Li and Z. Luo contributed to the experiments design, materials synthesis and characterization. Y. Zuo contributed to the electrochemical data analysis and discussion. C. Xing provided suggestions to the manuscript discussions. J. Llorca conducted XPS measurement and analysis. J. Arbiol performed the structural and compositional characterization of the materials by means of HRTEM and EELS and discussed the results. K. Pan and Y. Xie conducted the DFT calculations and the discussion.

Conflicts of interest

The authors declare no competing financial interest.

Acknowledgements

This work was supported by the European Regional Development Funds and by the Spanish Ministerio de Economíay Competitividad through the project SEHTOP, ENE2016- 77798-C4-3-R, and ENE2017-85087-C3. X.Y. thanks the China Scholarship Council for the scholarship support. J. Li obtained International Postdoctoral Exchange Fellowship Program (Talent-Introduction program) in 2019 and is grateful for the project (2019M663468) funded by the China Postdoctoral Science Foundation. Authors acknowledge funding from Generalitat de Catalunya 2017 SGR 327 and 2017 SGR 1246. ICN2 acknowledges the support from the Severo Ochoa Programme (MINECO, grant no. SEV-2017-0706) and is funded by the CERCA Programme/Generalitat de Catalunya. J. Llorca is a Serra Húnter Fellow and is grateful to MICINN/FEDER RTI2018-093996-B-C31, GC 2017 SGR 128 and to ICREA Academia program.

References

[1] C. Lamy, E.M. Belgsir, J.M. Leger, Electrocatalytic oxidation of aliphatic alcohols : Application to the direct alcohol fuel cell (DAFC), J. Appl. Electrochem. 31 (2001) 799–809.

[2] C. Lamy, A. Lima, V. LeRhun, F. Delime, C. Coutanceau, J. Le, Recent advances in the development of direct alcohol fuel cells (DAFC), J. Power Sources. 105 (2002) 283–296.

[3] E. Antolini, E.R. Gonzalez, Alkaline direct alcohol fuel cells, J. Power Sources. 195 (2010) 3431–3450. https://doi.org/10.1016/j.jpowsour.2009.11.145.

[4] E. Antolini, Catalysts for direct ethanol fuel cells, J. Power Sources. 170 (2007) 1–12. https://doi.org/10.1016/j.jpowsour.2007.04.009.

[5] M.A.F. Akhairi, S.K. Kamarudin, Catalysts in direct ethanol fuel cell (DEFC): An overview, Int. J. Hydrogen Energy. 41 (2016) 4214–4228. https://doi.org/10.1016/j.ijhydene.2015.12.145.

[6] C. Bianchini, P.K. Shen, Palladium-Based Electrocatalysts for Alcohol Oxidation in Half Cells and in Direct Alcohol Fuel Cells, Chem. Rev. 109 (2009) 4183–4206.

[7] M. Iqbal, Y.V. Kaneti, J. Kim, B. Yuliarto, Y.-M. Kang, Y. Bando, Y. Sugahara, Y. Yamauch, Chemical Design of Palladium-Based Nanoarchitectures for Catalytic Applications, Small. (2019) 1804378. https://doi.org/10.1002/smll.201804378.

[8] L.P.R. Moraes, B.R. Matos, C. Radtke, E.I. Santiago, F.C. Fonseca, S.C. Amico, C.F. Malfatti, Synthesis and performance of palladium-based electrocatalysts in alkaline direct ethanol fuel cell, Int. J. Hydrogen Energy. 41 (2016) 6457–6468. https://doi.org/10.1016/j.ijhydene.2016.02.150.

[9] F. Zhu, G. Ma, Z. Bai, R. Hang, B. Tang, Z. Zhang, X. Wang, High activity of carbon nanotubes supported binary and ternary Pd-based catalysts for methanol, ethanol and formic acid, J. Power Sources. 242 (2013) 610–620. https://doi.org/10.1016/j.jpowsour.2013.05.145.

[10] S.G. da Silva, M.H.M.T. Assumpção, J.C.M. Silva, R.F.B. De Souza, E. V. Spinacé, A.O. Neto, G.S. Buzzo, PdSn/C electrocatalysts with different atomic ratios for ethanol electro-oxidation in alkaline media, Int. J. Electrochem. Sci. 9 (2014) 5416–5424.

[11] A.N. Geraldes, D. Furtunato Da Silva, J.C. Martins Da Silva, O. Antonio De Sá, E.V. Spinacé, A.O. Neto, M. Coelho Dos Santos, Palladium and palladium-tin supported on multi wall carbon nanotubes or carbon for alkaline direct ethanol fuel cell, J. Power Sources. 275 (2015) 189–199. https://doi.org/10.1016/j.jpowsour.2014.11.024.

[12] C. Wang, Y. Wu, X. Wang, L. Zou, Z. Zou, H. Yang, Low temperature and surfactant-free synthesis of Pd2Sn intermetallic nanoparticles for ethanol electro-oxidation, Electrochim. Acta. 220 (2016) 628–634. https://doi.org/10.1016/j.electacta.2016.10.094.

[13] J. Liu, Z. Luo, J. Li, X. Yu, J. Llorca, D. Nasiou, Applied Catalysis B : Environmental Graphene-supported palladium phosphide PdP 2 nanocrystals for ethanol electrooxidation, Appl. Catal. B Environ. 242 (2019) 258–266. https://doi.org/10.1016/j.apcatb.2018.09.105.

[14] F. Wang, H. Xue, Z. Tian, W. Xing, L. Feng, Fe2P as a novel e fficient catalyst promoter in Pd/C system for formic acid electro-oxidation in fuel cells reaction, J. Power Sources. 375 (2018) 37–42. https://doi.org/10.1016/j.jpowsour.2017.11.055.

[15] P. Li, H.C. Zeng, Bimetallic Ni-Fe phosphide nanocomposites with a controlled architecture and composition enabling, (2018) 2231–2238. https://doi.org/10.1039/c7ta10665c.

[16] J. Liu, Z. Luo, J. Li, X. Yu, J. Llorca, D. Nasiou, Graphene-supported palladium phosphide PdP2 nanocrystals for ethanol electrooxidation, Appl. Catal. B Environ. 242 (2019) 258–266. https://doi.org/10.1016/j.apcatb.2018.09.105.

[17] A.R.J. Kucernak, K.F. Fahy, V.N.N. Sundaram, Facile synthesis of palladium phosphide electrocatalysts and their activity for the hydrogen oxidation , hydrogen evolutions , oxygen reduction and formic acid oxidation reactions, 262 (2016) 48–56.

[18] J. Liu, M. Meyns, T. Zhang, J. Arbiol, A. Cabot, A. Shavel, Triphenyl Phosphite as the Phosphorus Source for the Scalable and Cost-E ff ective Production of Transition Metal Phosphides, (2018). https://doi.org/10.1021/acs.chemmater.8b00290.

[19] B. Qiu, L. Cai, Y. Wang, Z. Lin, Y. Zuo, M. Wang, Fabrication of Nickel – Cobalt Bimetal Phosphide Nanocages for Enhanced Oxygen Evolution Catalysis, Adv. Funct. Mater. 28 (2018) 1706008. https://doi.org/10.1002/adfm.201706008.

[20] J. Ma, Y. Chen, L. Chen, L. Wang, Ternary Pd – Ni – P nanoparticle-based nonenzymatic glucose sensor with greatly enhanced sensitivity achieved through active-site engineering, Nano Res. 10 (2017) 2712–2720. https://doi.org/10.1007/s12274-017-1474-x.

[21] H. Liang, C. Xia, Q. Jiang, A.N. Gandi, U. Schwingenschlögl, Low temperature synthesis of ternary metal phosphides using plasma for asymmetric supercapacitors, Nano Energy. 35 (2017) 331–340. https://doi.org/10.1016/j.nanoen.2017.04.007.

[22] R. Jiang, D.T. Tran, J.P. Mcclure, D. Chu, A Class of (Pd-Ni-P) Electrocatalysts for the Ethanol Oxidation Reaction in Alkaline Media, ACS Catal. 4 (2014) 2577–2586. https://doi.org/10.1021/cs500462z.

[23] J. Chang, L. Feng, C. Liu, W. Xing, X. Hu, An Effective Pd-Ni2P/C Anode Catalyst for Direct Formic Acid Fuel Cells, Angew.Chem. Int. Ed. 53 (2014) 122–126. https://doi.org/10.1002/anie.201308620.

[24] L. Feng, H. Xue, Advances in Transition-Metal Phosphide Applications in Electrochemical Energy Storage and Catalysis, (2017) 20–34. https://doi.org/10.1002/celc.201600563.

[25] Z. Luo, J. Lu, C. Flox, R. Nafria, A. Genç, J. Arbiol, J. Llorca, M. Ibáñez, J.R. Morante, A. Cabot, Pd2Sn [010] nanorods as a highly active and stable ethanol oxidation catalyst, J. Mater. Chem. A. 4 (2016) 16706–16713. https://doi.org/10.1039/c6ta06430b.

[26] L. Bu, N. Zhang, S. Guo, X. Zhang, J. Li, J. Yao, T. Wu, G. Lu, J.Y. Ma, D. Su, Biaxially Strained PtPb/Pt Core/Shell Nanoplate Boosts Oxygen Reduction Catalysis, Science (80-.). 354 (2016) 1410.

[27] G. Kresse, J. Hafner, Ab initio melecular dynamics for liquid metals, Phys. Rev. B. 47 (1993) 558–561.

[28] G. Kresse, J. Hafner, Ab initio melecular-dynamics simulation of the liquid-metal —amorphous-semiconductor transition in germanium, Phsical Rev. B. 49 (1994) 14251–14269.

[29] G. Kresse, J. Furthmu, Efficient iterative schemes for ab initio total-energy calculations using a plane-wave basis set, Phys. Rev. B. 54 (1996) 11169–11186.

[30] G. Kresse, J. Furthmiiller, Efficiency of ab-initio total energy calculations for metals and semiconductors using a plane-wave basis set, Comput. Mater. Sci. 6 (1996) 15–50.

[31] J.. Perdew, K. Burke, M. Ernzerhof, Generalized Gradient Approximation Made Simple, Phys. Rev. Lett. 77 (1996) 3865–3868.

[32] Projector augmented-wave method, Phys. Rev. B. 50 (1994) 17953–17979.

[33] H.J. Monkhorst, J.D. Pack, Special points for Brillouin-zone integrations, Phys. Rev. B. 13 (1976) 5188–5192.

[34] J.C. Phys, S. Grimme, J. Antony, S. Ehrlich, H. Krieg, A consistent and accurate ab initio parametrization of density functional dispersion correction (DFT-D) for the 94 elements H-Pu, J. Chem. Phys. 132 (2010) 154104. https://doi.org/10.1063/1.3382344.

[35] S. Grimme, S. Ehrlich, L. Goerigk, Effect of the Damping Function in Dispersion Corrected Density Functional Theory, J. Comput. Chem. 32 (2011) 1456–1465. https://doi.org/10.1002/jcc.

[36] Y. Luo, X. Li, X. Cai, X. Zou, F. Kang, H. Cheng, B. Liu, Two-Dimensional MoS2 Confined Co(OH)2 Electrocatalysts for Hydrogen Evolution in Alkaline Electrolytes, ACS Nano. 12 (2018) 4565–4573. https://doi.org/10.1021/acsnano.8b00942.

[37] J.F. Moulder, W.F. Stickle, P.E. Sobol, K.D. Bomben, Handbook of X-ray Photoelectron Spectroscopy: A Reference Book of Standard Spectra for Identification and Interpretation of XPS Data, 1992.

[38] Z. Luo, J. Lu, C. Flox, R. Nafria, A. Genç, J.R. Morante, A. Cabot, Pd2Sn[010]nanorods as a highly active and stable ethanol oxidation catalyst, J.Mater.Chem.A. 4 (2016) 16706–16713. https://doi.org/10.1039/c6ta06430b.

[39] J. Liu, S. Wang, K. Kravchyk, M. Ibáñez, D. Nasiou, M. Me-, J. Llorca, J. Arbiol, M. V Kovalenko, A. Cabot, SnP nanocrystals as anode material for Na-ion battery, J.Mater.Chem.A. 6 (2018) 10958–10966.

[40] E. Capacitors, What Are Batteries , Fuel Cells , and Supercapacitors ?, Chem. Rev. 104 (2004) 4245–4269. https://doi.org/10.1021/cr020730k.

[41] Z.X. Liang, T.S. Zhao, J.B. Xu, L.D. Zhu, Electrochimica Acta Mechanism study of the ethanol oxidation reaction on palladium in alkaline media, 54 (2009) 2203–2208. https://doi.org/10.1016/j.electacta.2008.10.034.

[42] J. Liu, Y. Zheng, Z. Hong, K. Cai, F. Zhao, H. Han, Microbial synthesis of highly dispersed PdAu alloy for enhanced electrocatalysis, Sci. Adv. (2016) e1600858.

[43] J. Liu, Z. Huang, K. Cai, H. Zhang, Z. Lu, T. Li, Y. Zuo, H. Han, Clean Synthesis of an Economical 3D Nanochain Network of PdCu Alloy with Enhanced Electrocatalytic Performance towards Ethanol Oxidation, Chem.Eur.J. 21 (2015) 17779–17785. https://doi.org/10.1002/chem.201503432.

[44] X. Zhao, L. Dai, Q. Qin, F. Pei, C. Hu, N. Zheng, Self-Supported 3D PdCu Alloy Nanosheets as a Bifunctional Catalyst for Electrochemical Reforming of Ethanol, Small. 13 (2017) 1602970. https://doi.org/10.1002/smll.201602970.

[45] C. Bi, C. Feng, T. Miao, Y. Song, D. Wang, H. Xia, Understanding the e ff ect of ultrathin AuPd alloy shells of irregularly shaped Au@AuPd nanoparticles with high-index facets on enhanced, Nanoscale. 7 (2015) 20105–20116. https://doi.org/10.1039/c5nr06035d.

[46] Y. Shu, X. Shi, Y. Ji, Y. Wen, X. Guo, Y. Ying, Y. Wu, H. Yang, Hollow Echinus-like PdCuCo Alloy for Superior Efficient Catalysis of Ethanol, ACS Appl.Mater.Interfaces. 10 (2018) 4743–4749. https://doi.org/10.1021/acsami.7b17731.

[47] X. Yu, Z. Luo, T. Zhang, P. Tang, J. Li, X. Wang, J. Llorca, J. Arbiol, J. Liu, A. Cabot, Stability of Pd3Pb Nanocubes during Electrocatalytic Ethanol Oxidation, Chem.Mater. 32 (2020) 2044–2052. https://doi.org/10.1021/acs.chemmater.9b05094.

[48] P. Wu, Y. Huang, L. Zhou, Y. Wang, Y. Bu, J. Yao, Nitrogen-doped graphene supported highly dispersed palladium-lead nanoparticles for synergetic enhancement of ethanol electrooxidation in alkaline medium, Electrochim. Acta. 152 (2015) 68–74. https://doi.org/10.1016/j.electacta.2014.11.110.

[49] J. Yang, Y. Xie, R. Wang, B. Jiang, C. Tian, G. Mu, J. Yin, B. Wang, H. Fu, Synergistic Effect of Tungsten Carbide and Palladium on Graphene for Promoted Ethanol Electrooxidation, ACS Appl.Interfaces. 5 (2013) 6571–6579. https://doi.org/10.1021/am401216s.

[50] Y. Wang, Q. He, J. Guo, J. Wang, Z. Luo, T.D. Shen, K. Ding, A. Khasanov, S. Wei, Z. Guo, Ultra fine FePd Nanoalloys Decorated Multiwalled Cabon Nanotubes toward Enhanced Ethanol Oxidation Reaction, ACS Appl.Mater.Interfaces. 7 (2015) 23920–23931. https://doi.org/10.1021/acsami.5b06194.

[51] S. Fu, C. Zhu, D. Du, Y. Lin, Facile One-Step Synthesis of Three-Dimensional Pd-Ag Bimetallic Alloy Networks and Their Electrocatalytic Activity toward Ethanol Oxidation, ACS Appl.Mater.Interfaces. 7 (2015) 13842–13848. https://doi.org/10.1021/acsami.5b01963.

[52] D. Bin, B. Yang, K. Zhang, C. Wang, J. Wang, J. Zhong, Design of PdAg Hollow Nanoflowers through Galvanic Replacement and Their Application for Ethanol Electrooxidation, Chem.Eur.J. 22 (2016) 16642–16647. https://doi.org/10.1002/chem.201601544.

[53] K. Zhang, D. Bin, B. Yang, C. Wang, F. Ren, Y. Du, Ru-assisted synthesis of Pd/Ru nanodendrites with high activity for ethanol electrooxidation, Nanoscale. 7 (2015) 12445–12451. https://doi.org/10.1039/c5nr02713f.

[54] F. Guo, Y. Li, B. Fan, Y. Liu, L. Lu, Y. Lei, Carbon- and Binder-Free Core- Shell Nanowire Arrays for E fficient Ethanol Electro-Oxidation in Alkaline Medium, ACS Appl.Mater.Interfaces. 10 (2018) 4705–4714. https://doi.org/10.1021/acsami.7b16615.

[55] J. Xue, G. Han, W. Ye, Y. Sang, H. Li, P. Guo, X.S. Zhao, Structural Regulation of PdCu 2 Nanoparticles and Their Electrocatalytic Performance for Ethanol Oxidation, ACS Appl.Mater.Interfaces. 8 (2016) 34497–34505. https://doi.org/10.1021/acsami.6b13368.

[56] S. Ye, J. Feng, G. Li, Pd Nanoparticle/CoP Nanosheet Hybrids: Highly Electroactive and Durable Catalysts for Ethanol Electrooxidation, ACS Catal. 6 (2016) 7962–7969. https://doi.org/10.1021/acscatal.6b02263.

[57] T. Miao, Y. Song, C. Bi, H. Xia, D. Wang, X. Tao, Correlation of Surface Ag Content in AgPd Shells of Ultrasmall Core-Shell Au@ AgPd Nanoparticles with Enhanced Electrocatalytic Performance for Ethanol Oxidation, J.Phys.Chem.C. 119 (2015) 18434–18443. https://doi.org/10.1021/acs.jpcc.5b05571.

[58] G. Zhang, J. Wu, B. Xu, Syntheses of Sub-30 nm Au@ Pd Concave Nanocubes and Pt-on-(Au@Pd) Trimetallic Nanostructures as Highly E ffi cient Catalysts for Ethanol Oxidation, J.Phys.Chem.C. 116 (2012) 20839–20847. https://doi.org/10.1021/jp304570c.

[59] S.C. Sarma, S.C. Peter, Understanding small-molecule electro-oxidation on palladium based compounds-a feature on experimental and theoretical approaches, Dalt. Trans. 47 (2018) 7864–7869. https://doi.org/10.1039/c8dt00443a.

[60] Z. Wu, B. Miao, E. Hopkins, K. Park, Y. Chen, H. Jiang, M. Zhang, C. Zhong, L. Wang, Poisonous Species in Complete Ethanol Oxidation Reaction on Palladium Catalysts, J. Phys. Chem. C. 123 (2019) 20853–20868. https://doi.org/10.1021/acs.jpcc.9b04229.

[61] L. Chen, L. Lu, H. Zhu, Y. Chen, Y. Huang, Y. Li, L. Wang, Improved ethanol electrooxidation performance by shortening Pd–Ni active site distance in Pd-Ni-P nanocatalysts, Nat. Commun. 8 (2017) 14136. https://doi.org/10.1038/ncomms14136.